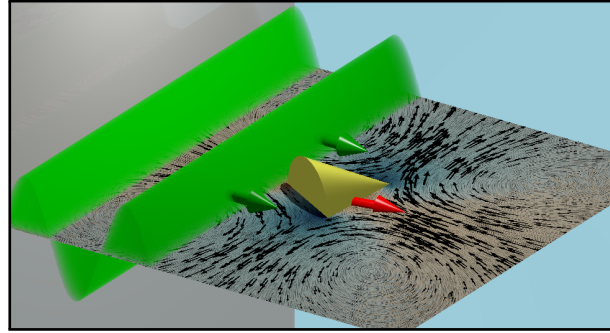


Orientation-dependent propulsion of cone-shaped nano- and microparticles by a traveling ultrasound wave

Johannes Voß¹ and Raphael Wittkowski^{1,*}

¹*Institut für Theoretische Physik, Center for Soft Nanoscience,
Westfälische Wilhelms-Universität Münster, D-48149 Münster, Germany*

Previous studies on ultrasound-propelled nano- and microparticles have considered only systems where the particle orientation is perpendicular to the direction of propagation of the ultrasound. However, in future applications of these particles, they will typically be able to attain also other orientations. Therefore, using direct acoustofluidic simulations, we here study how the propulsion of cone-shaped nano- and microparticles, which are known to have a particularly efficient acoustic propulsion and are therefore promising candidates for future applications, depends on their orientation relative to the propagation direction of a traveling ultrasound wave. Our results reveal that the propulsion of the particles depends strongly on their orientation relative to the direction of wave propagation and that the particles tend to orient perpendicularly to the wave direction. We also present the orientation-averaged translational and angular velocities of the particles, which correspond to the particles' effective propulsion for an isotropic exposure to ultrasound. Our results allow assessing how free ultrasound-propelled colloidal particles move in three spatial dimensions and thus constitute an important step towards the realization of the envisaged future applications of such particles.



I. INTRODUCTION

The experimental discovery of colloidal particles with fuel-free ultrasound propulsion in 2012 [1] made important applications of active particles [2] become within reach [3–6]. Especially in medicine [7–11], where such particles could be used, e.g., for targeted drug delivery [12, 13], and in materials science [14], where they could form active materials with exceptional properties [15, 16], ultrasound-propelled nano- and microparticles [1, 17–50] have great potential. Since acoustic propulsion is biocompatible and allows to supply the particles permanently with energy, ultrasound-propelled particles are more suitable for medical applications than other propulsion mechanisms that have been developed in the past [8, 51–55].

The great potential for applications of ultrasound-propelled nano- and microparticles resulted in an intensive investigation of their properties [1, 17–50, 56–66]. Most of the existing studies are experimental [1, 17–

26, 28–38, 40–42, 45–50, 57, 58, 60, 61, 64–66], a few of them are numerical [31, 36, 43, 44, 65, 66], and only two studies are analytical [56, 62]. The previous studies considered both rigid particles [1, 17, 18, 20–24, 28–30, 32, 35, 36, 38, 43, 44, 48–50, 56, 58, 60, 62, 64–66] and particles with movable components [31, 33, 37, 42, 45, 46, 53, 57]. In the former case, various particle shapes have been considered: cylinders with concave and convex ends [1, 17, 18, 20–24, 28, 30, 32, 35, 38, 48, 50, 62, 65], half-spheres [43], half-sphere cups (nanoshells) [29, 43, 66], cones [43, 44], and gear-shaped particles [36, 60]. Among the studied particles, cone-shaped ones have been shown to be particularly promising candidates for future research and applications, since they can easily be produced in large numbers and have relatively efficient propulsion [44]. Even hybrid particles combining acoustic propulsion with other propulsion mechanisms have been studied [49, 58, 61, 64–67]. Nevertheless, our understanding of ultrasound-propelled nano- and microparticles is still very incomplete.

One problem is that nearly all existing studies consider a standing ultrasound wave, although for future applications a traveling ultrasound wave is much more realistic [43, 44]. Another problem is that in the previous studies

* Corresponding author: raphael.wittkowski@uni-muenster.de

the particles are oriented perpendicular to the propagation direction of the ultrasound, although we can expect that in future applications the particles will be able to orient also differently when they move, e.g., within an active suspension forming an active material or within the vascular system of a patient. The reason for studying only perpendicular orientations so far is that in the experimental studies the particles are levitated in the nodal plane of a standing ultrasound wave, which is perpendicular to the propagation direction of the ultrasound wave and restricts the motion and orientation of the particles to that plane, and that the existing theoretical studies consider systems that are similar to those that have been investigated in experiments.

In this work, we go an important step further by studying the acoustic propulsion of particles that are exposed to a planar traveling ultrasound wave and that can orient in any direction relative to the ultrasound wave. Focusing on the promising cone-shaped particles, we study how their propulsion depends on the relative orientation of particle and ultrasound wave. For this purpose, we apply direct computational fluid dynamic simulations that are based on the compressible Navier-Stokes equations to calculate the propagation of the ultrasound and its interaction with a particle. These simulations yield the sound-induced forces and torques acting on the particle, which in turn determine its translational and angular propulsion velocity.

II. RESULTS AND DISCUSSION

We determined the time-averaged propulsion of a cone-shaped particle in water that is exposed to a planar traveling ultrasound wave with frequency $f = 1$ MHz and energy density $E = 22.7 \text{ mJ m}^{-3}$ for various orientations of the particle. The considered particle has diameter $\sigma = 2^{-1/2} \mu\text{m}$ and height $h = \sigma$ and the water is initially at standard temperature, under standard pressure, and quiescent. See Methods for details.

Figure 1 shows our results for the particle's translational propulsion velocity v_{\parallel} parallel to the orientation (i.e., symmetry axis) of the particle, the component v_{\perp} perpendicular to the particle's orientation, and the angular velocity ω relative to the particle's center of mass for orientations $\theta \in [0, \pi]$. At $\theta = 0$, the particle orientation and the propagation direction of the ultrasound are parallel, and at $\theta = \pi$, they are antiparallel. Remarkably, the considered ultrasound-propelled particle has orientation-dependent propulsion.

The velocity component v_{\parallel} starts with a local minimum $v_{\parallel} = -0.032(7) \mu\text{m s}^{-1}$ at $\theta = 0$. This means that for a particle that is oriented parallel to the ultrasound wave, the velocity component v_{\parallel} moves the particle backwards and thus antiparallel to the ultrasound. v_{\parallel} then increases, changes its sign between $\theta = \pi/6$ and $\theta = \pi/3$, and further increases until it reaches its maximum $v_{\parallel} = 0.072(7) \mu\text{m s}^{-1}$ at $\theta = \pi/2$ where particle and ul-

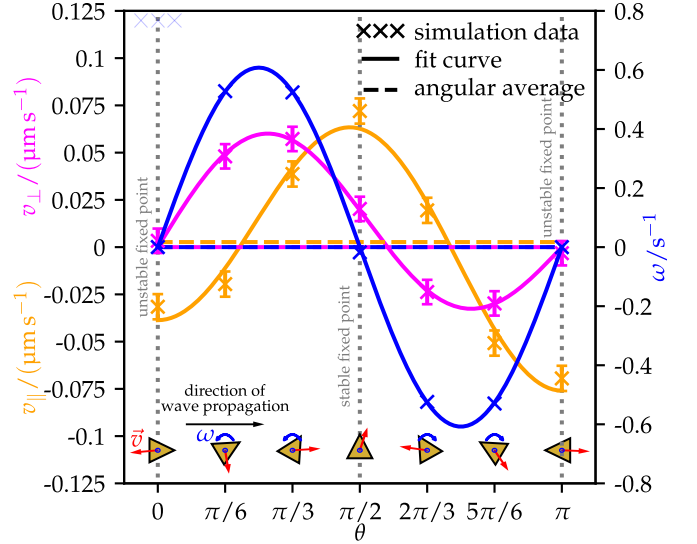


FIG. 1. Simulation data and fit curves for the translational velocity components v_{\parallel} and v_{\perp} parallel and perpendicular to the orientation of a cone-shaped particle, respectively, as well as the particle's angular velocity ω for various orientations of the particle. In addition, the orientationally averaged values of v_{\parallel} , v_{\perp} , and ω , as well as fixed points of the particle orientation, are shown. See Ref. [68] for the raw data corresponding to this figure.

ζ	$a_{\zeta,0}$	$a_{\zeta,1}$	$a_{\zeta,2}$
\parallel	$0.002\,691 \mu\text{m s}^{-1}$	$0.018\,64 \mu\text{m s}^{-1}$	$-0.059\,99 \mu\text{m s}^{-1}$
\perp	—	$0.019\,49 \mu\text{m s}^{-1}$	$0.091\,69 \mu\text{m s}^{-1}$

TABLE I. Fit parameters for the velocity components v_{ζ} with $\zeta \in \{\parallel, \perp\}$. See Fig. 3 for their definitions.

trasound are oriented perpendicularly. Hence, in the situation of all the previous studies on ultrasound-propelled particles, where the particles are perpendicular to the ultrasound, the particles considered in the present work exhibit their fastest forward motion. For even larger values of the angle θ , v_{\parallel} decreases again. Between $\theta = 2\pi/3$ and $\theta = 5\pi/6$ it changes sign for the second time and it reaches its global minimum $v_{\parallel} = -0.069(7) \mu\text{m s}^{-1}$ at $\theta = \pi$. Here, the particle again moves backward, which now means parallel to the ultrasound. To find a simple function that interpolates the simulation data for v_{\parallel} , we take into account that it must have the symmetry property $v_{\parallel}(\theta) = v_{\parallel}(-\theta)$ to reflect the symmetry of the particle shape. We, therefore, use the second-order Fourier series

$$v_{\parallel}(\theta) = a_{\parallel,0} + a_{\parallel,1} \cos(\theta) + a_{\parallel,2} \cos(2\theta), \quad (1)$$

which is in good agreement with the simulation results. The values of the expansion coefficients $a_{\parallel,0}$, $a_{\parallel,1}$, and $a_{\parallel,2}$ that result from fitting the function (1) to the experimental data are given in Tab. I. An angular average

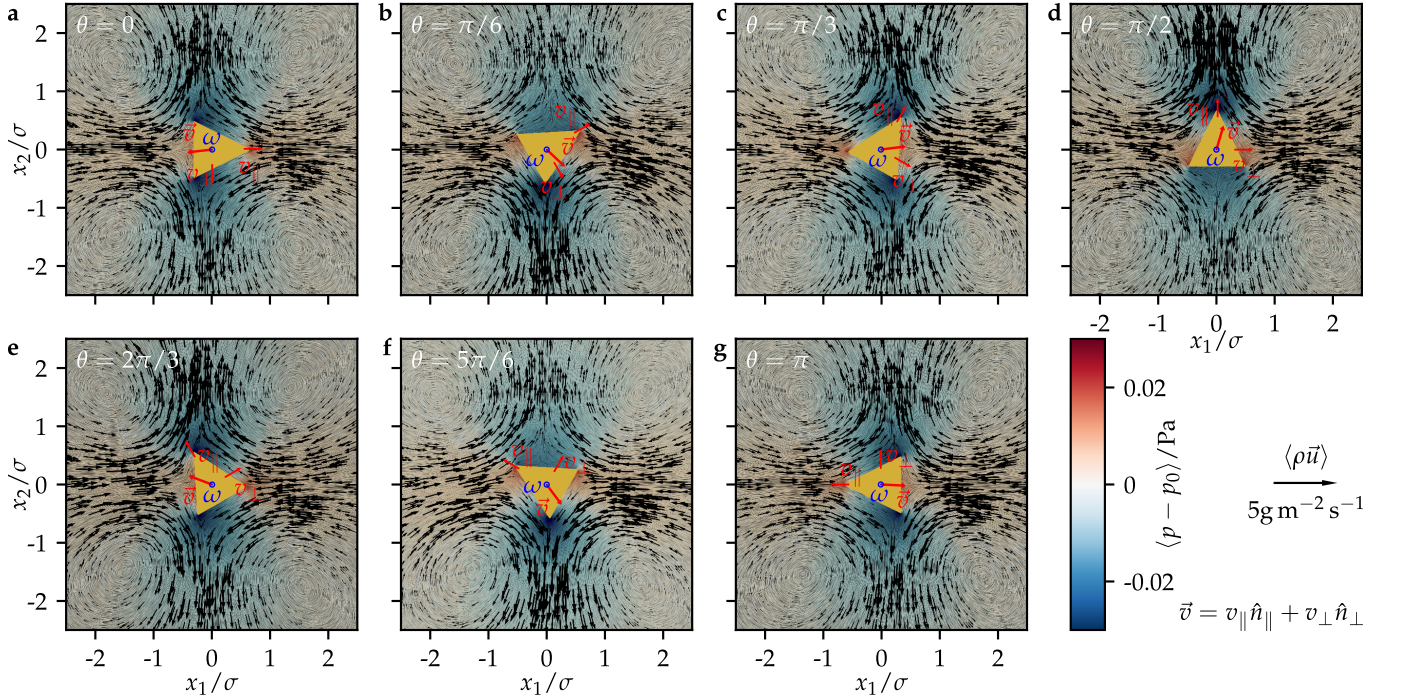


FIG. 2. The time-averaged mass-current density $\langle \rho \vec{u} \rangle$ and reduced pressure $\langle p - p_0 \rangle$ as well as the translational propulsion velocity $\vec{v} = v_{\parallel} \hat{n}_{\parallel} + v_{\perp} \hat{n}_{\perp}$ and angular propulsion velocity ω for all considered orientations of the particle, where ρ , \vec{u} , and p are the fluid's mass density field, velocity field, and pressure field, respectively, and \hat{n}_{\parallel} and \hat{n}_{\perp} are orientation vectors that are parallel and perpendicular to the particle orientation, respectively. See Ref. [68] for the raw data corresponding to this figure.

of v_{\parallel} yields

$$\langle v_{\parallel} \rangle_{\theta} = \frac{1}{2\pi} \int_0^{2\pi} v_{\parallel}(\theta) d\theta = a_{\parallel,0} = 0.00269 \mu\text{m s}^{-1}. \quad (2)$$

This means that for an isotropic ultrasound field, the particle will move forward.

For the velocity component v_{\perp} , qualitatively different behavior is observed. This component vanishes at $\theta = 0$ for reasons of symmetry, meaning that there is no motion perpendicular to the ultrasound wave when the particle is oriented parallel to the propagation direction of the ultrasound. When θ increases, the value of v_{\perp} increases until a maximum is reached between $\theta = \pi/6$, where $v_{\perp} = 0.048(7) \mu\text{m s}^{-1}$, and $\theta = \pi/3$, where $v_{\perp} = 0.057(7) \mu\text{m s}^{-1}$. Afterwards, v_{\perp} decreases, changes its sign between $\theta = \pi/2$ and $\theta = 2\pi/3$, and reaches its minimum between $\theta = 2\pi/3$, where $v_{\perp} = -0.024(7) \mu\text{m s}^{-1}$, and $\theta = 5\pi/6$, where $v_{\perp} = -0.030(7) \mu\text{m s}^{-1}$. For larger angles θ , the component v_{\perp} increases again until it vanishes at $\theta = \pi$ for reasons of symmetry. This means that when the particle's orientation has a component parallel to the propagation direction of the ultrasound, the velocity component v_{\perp} contributes to a parallel motion of the particle, whereas for an orientation with a moderate or large antiparallel component v_{\perp} contributes to an antiparallel motion. Note that due to numerical inaccuracies in the calculations, the values of v_{\perp} are not exactly zero at $\theta = 0$ and $\theta = \pi$. For interpolating the simulation results for v_{\perp} , we take into account the symmetry

property $v_{\perp}(\theta) = -v_{\perp}(-\theta)$ that results from the setup of the considered system and use the simple function

$$v_{\perp}(\theta) = a_{\perp,1} \sin(\theta) + a_{\perp,2} \sin(\theta) \cos(\theta) \quad (3)$$

that is in good agreement with the simulation data. The values of the expansion coefficients $a_{\perp,1}$ and $a_{\perp,2}$ that result from fitting this function to the simulation data are given in Tab. I. For reasons of symmetry, the orientation-averaged velocity $\langle v_{\perp} \rangle_{\theta}$ vanishes.

For the angular velocity ω , we find a qualitatively similar behavior as for v_{\perp} , but ω vanishes also for $\theta = \pi/2$, although this follows not directly from symmetry considerations. The particle therefore rotates anticlockwise for angles $0 < \theta < \pi/2$ and clockwise for $\pi/2 < \theta < \pi$. This means that there are unstable fixed points of the particle orientation at $\theta = 0$ and $\theta = \pi$ and a stable fixed point at $\theta = \pi/2$. The particle thus tends to orient perpendicular to the direction of ultrasound propagation. It is interesting that a perpendicular alignment of the particle, which has been observed in experiments with standing ultrasound waves [1, 17, 22, 29, 30, 36, 48, 50, 66], occurs also here, where a traveling ultrasound wave is chosen. Using the rotational diffusion coefficient $D_R = 1.78 \text{ s}^{-1}$ of the particle that is considered in the present work, which is equivalent to a reorientation of the particle within 0.56 s, and comparing it with the maximal observed angular velocity of $\omega = 0.53 \text{ s}^{-1}$, which implies a rotation by $\pi/2$ within about 1 s, we find that the reorientation of a particle by rotational propulsion is of the same order of magni-

tude as the reorientation by Brownian motion. Note that this applies to the energy density of the ultrasound that is chosen in this work. For lower or higher ultrasound intensities, Brownian motion or active rotation dominate, respectively. To interpolate the simulation data for ω , we use the function

$$\omega(\theta) = 0.6079 \sin(2\theta) \text{ s}^{-1}, \quad (4)$$

where the value of the prefactor is determined by fitting the function to the simulation data. Again, the agreement with the simulation data is good. The orientational average $\langle \omega \rangle_\theta$ of the angular velocity vanishes for reasons of symmetry.

Assuming that the propulsion velocities of the particle are proportional to the energy density of the ultrasound, which is suggested by the fact that both the translational propulsion velocity [31] and the energy density of the ultrasound [69] have been found to be proportional to the square of the driving voltage, we can estimate the values of the propulsion velocities for a higher ultrasound intensity. Increasing the energy density from $E = 22.7 \text{ mJ m}^{-3}$, which corresponds to our simulations, to $E_{\text{max}} = 4.9 \text{ J m}^{-3}$, which is the maximal energy density that is allowed by the U.S. Food and Drug Administration for diagnostic applications of ultrasound in the human body [70], can then be expected to lead to an increase of v_\parallel , v_\perp , and ω by a factor of about 216. The orientationally averaged propulsion should then equal a forward propulsion speed $\langle v_\parallel \rangle_{\theta, \text{rescaled}} \approx 0.6 \mu\text{m s}^{-1}$. Finally, we consider the flow field around the particle for different orientations. This is important to clarify whether the flow field around such an ultrasound-propelled particle is similar to that of a squirmer, which has been suggested by a recent study [43]. This study found a squirmer-like flow field for different particles but considered only particle orientations perpendicular to the direction of ultrasound propagation. Our results for the flow field are shown in Fig. 2. Interestingly, the flow field looks qualitatively similar irrespective of the orientation of the particle. This reveals that these particles cannot be considered as squirmers.

III. CONCLUSIONS

Our investigation of the motion of a cone-shaped particle that is propelled by a planar traveling ultrasound wave and has a variable orientation relative to the propagation direction of the ultrasound resulted in several important observations.

First, we found that the propulsion of the particle depends on its orientation. This is a feature that affects the dynamics of the particle in an interesting way, as has recently been addressed using particles with a different propulsion mechanism [71].

Second, we revealed the particular orientation-dependence of the propulsion and provided simple analytical expressions for it. Knowledge of this dependence

is very important with respect to future applications of acoustically propelled particles, e.g., in nanomedicine or materials science, where the particles will be able to attain various or all directions relative to the (typically traveling) ultrasound wave. Compared to the previous studies from the literature that consider only particles that are perpendicular to a (standing) ultrasound wave, the present work thus constitutes a large step forward. Furthermore, the provided functions for the orientation-dependence of the propulsion can be used to model this propulsion when describing the behavior of the particles via Langevin equations [72, 73] or field theories [74–76]. For the future investigation of ultrasound-propelled nano- and microparticles, such a description would be highly advantageous, since its characteristic time scale can be orders of magnitude larger than the period of the ultrasound, which would strongly reduce the effort to study the particles' dynamics on times scales of seconds to hours as they correspond to experiments with such particles.

Third, we observed that, depending on the orientation of the particle, the velocity vector can show in any direction including an orientation antiparallel to the wave propagation. Also this finding is highly important with respect to applications, since it shows that the ultrasound-propelled particles can move even towards the source of the ultrasound.

Fourth, we found that the orientation of the particle has three fixed points including two unstable ones and a stable one, where the latter fixed point corresponds to a particle orientation that is perpendicular to the ultrasound wave. This shows that the observation of previous studies [1, 17, 22, 29, 30, 36, 48, 50, 66], that the particles align within the nodal plane of a standing ultrasound wave, is not simply a result of the particles' levitation in the nodal plane but, at least partially, a result of an alignment mechanism that is present also for traveling ultrasound waves. This alignment mechanism is interesting since it provides new opportunities to steer acoustically propelled particles.

Fifth, our results show a nonzero orientation-averaged forward propulsion of the particle. In an isotropic ultrasound field, the particle will therefore move forward irrespective of its orientation. This is an important finding since it shows that acoustically-propelled particles can move also simply by forward translation without rotational propulsion, like the idealized active particles that are primarily studied in the literature [2, 74, 75, 77–79]. Such ultrasound-propelled particles can therefore be applied also in situations where purely translational propulsion is required (e.g., when performing experiments that correspond to the aforementioned studies), when the ultrasound supply is designed accordingly.

Sixth, we observed that the flow field around the particle looks rather similar for all of its orientations. This means that the particle cannot be described as a pusher, as has been assumed previously [43]. On the other hand, it seems that one can describe the flow field by a pusher-

like flow field that translates with the particle but has a fixed orientation. Based on this model for the flow field, it should be possible to determine the locally time-averaged hydrodynamic interactions between different ultrasound-propelled particles when they are not too close together.

In summary, this work solves problems and provides new insights that are highly important on the way towards the intriguing applications that have been envisaged for ultrasound-propelled nano- and microparticles [7–16]. In the future, this work should be continued by varying the particle shape, particle size, ultrasound frequency, ultrasound intensity, and other parameters of the system and studying how this affects, e.g., the orientation-averaged propulsion velocity or the fixed points of the particle orientation.

IV. METHODS

Figure 3 shows and explains the setup chosen for our simulations. We use a rectangular simulation domain with width $2l_1$ and height $l_2 = 200 \mu\text{m}$ that is aligned with the coordinate system so that the width is along the x_1 axis and the height along the x_2 axis. The simulation domain is filled with water that initially is at standard temperature $T_0 = 293.15 \text{ K}$ and standard pressure $p_0 = 101325 \text{ Pa}$ and has a vanishing velocity field $\vec{u}_0 = 0 \text{ m s}^{-1}$. In the middle of the simulation domain, a cone-shaped particle with diameter $\sigma = 2^{-1/2} \mu\text{m}$, height $h = \sigma$, and particle domain Ω_p is placed such that the center of masses S of simulation domain and particle coincide. A planar traveling ultrasound wave with frequency $f = 1 \text{ MHz}$ enters the simulation domain at the left boundary (the inlet), propagates in the x_1 direction, interacts with the particle, and leaves the domain at the right boundary (the outlet). The ultrasound wave entering the system at the inlet is described by the time-dependent velocity $u_{\text{in}}(t) = (\Delta p / (\rho_0 c_f)) \sin(2\pi f t)$ and pressure $p_{\text{in}}(t) = \Delta p \sin(2\pi f t)$ with the pressure amplitude $\Delta p = 10 \text{ kPa}$ and the mass density $\rho_0 = 998 \text{ kg m}^{-3}$ and sound velocity $c_f = 1484 \text{ m s}^{-1}$ of the unperturbed fluid. This ultrasound wave has an acoustic energy density $E = \Delta p^2 / (2\rho_0 c_f^2) = 22.7 \text{ mJ m}^{-3}$. We choose the width of the simulation domain so that $l_1 = \lambda/4$, where $\lambda = 1.484 \text{ mm}$ is the wavelength of the ultrasound. The orientation of the particle is described by an angle θ that is measured from the positive x_1 axis to the vector that runs from S to the tip of the particle that is on its axis of symmetry. We vary the orientation from $\theta = 0$, where the particle points in the direction of propagation of the ultrasound, to $\theta = \pi$, where the particle and the ultrasound wave point in opposite directions. The ultrasound exerts time-averaged propulsion forces F_{\parallel} and F_{\perp} parallel and perpendicular to the particle orientation, respectively, and a time-averaged propulsion torque T on the particle. F_{\parallel} , F_{\perp} , and T act on S . We denote the directions parallel and perpendicular to the particle by

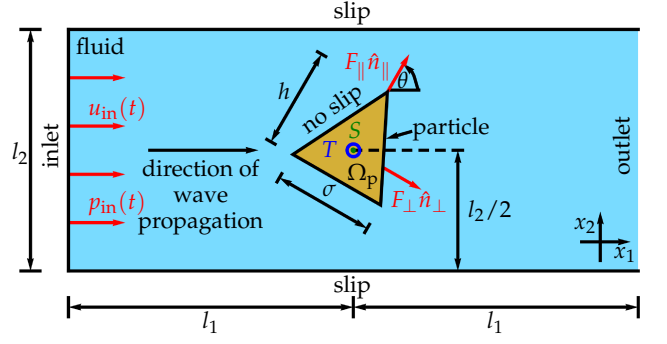


FIG. 3. Setup for the simulations. The simulation domain has width (parallel to the x_1 axis of our coordinate system) $2l_1$ and height (parallel to the x_2 axis) l_2 and is filled with water as fluid. At the left boundary of the rectangular fluid domain, the inlet, a planar ultrasound wave enters the system and propagates in the x_1 direction. We prescribe the incoming ultrasound wave at this boundary by a time-dependent inflow velocity $u_{\text{in}}(t)$ and inflow pressure $p_{\text{in}}(t)$. In the middle of the fluid domain, a rigid cone-shaped particle is placed so that the center of mass S of the particle and that of the fluid domain coincide. This particle shape is chosen since it corresponds to a fast forward motion [44]. The particle constitutes a particle domain Ω_p . It has diameter σ , height h , and orientation angle θ . We measure the angle θ in such a way that it describes the orientation of the particle, which is here defined as the orientation of the unit vector \hat{n}_{\parallel} that is parallel to the particle's symmetry axis and points from S towards one tip of the particle, relative to the incoming ultrasound wave. For $\theta = 0$, the particle's orientation \hat{n}_{\parallel} is parallel to the direction of wave propagation, for $\theta = \pi/2$ they are perpendicular, and for $\theta = \pi$, they are antiparallel. We define also an orientational unit vector \hat{n}_{\perp} that is always perpendicular to \hat{n}_{\parallel} and for $\theta = \pi/2$ parallel to the direction of wave propagation. The interaction of the ultrasound with the particle results in a time-averaged propulsion force with components F_{\parallel} parallel to \hat{n}_{\parallel} and F_{\perp} parallel to \hat{n}_{\perp} as well as in a time-averaged propulsion torque T acting at S . At the right boundary of the fluid domain, the outlet, the ultrasound can leave the system. We use slip boundary conditions for the boundaries of the fluid domain that are parallel to the x_1 direction and no-slip boundary conditions for the boundary of the particle.

orientational unit vectors

$$\hat{n}_{\parallel} = (\cos(\theta), \sin(\theta))^T, \quad (5)$$

$$\hat{n}_{\perp} = (\sin(\theta), -\cos(\theta))^T, \quad (6)$$

respectively, where \hat{n}_{\perp} points in the negative x_2 direction for $\theta = 0$. For the boundaries of the simulation domain parallel to the x_1 axis, we use a slip boundary condition, and for the boundary of the particle, we use a no-slip boundary condition. The parameters of the system that are relevant for our simulations and the values assigned to these parameters are summarized in Tab. II.

In our simulations, we solve a set of coupled partial differential equations consisting of the continuity equation for the mass-density field of the fluid, the compressible

Name	Symbol	Value
Particle diameter	σ	$2^{-1/2}\mu\text{m}$
Particle height	h	σ
Particle orientation angle	θ	$0-\pi$
Sound frequency	f	1 MHz
Speed of sound	c_f	1484 m s^{-1}
Time period of sound	$\tau = 1/f$	1 μs
Wavelength of sound	$\lambda = c_f/f$	1.484 mm
Temperature of fluid	T_0	293.15 K
Mean mass density of fluid	ρ_0	998 kg m^{-3}
Mean pressure of fluid	p_0	101 325 Pa
Initial velocity of fluid	\vec{u}_0	$\vec{0}\text{ m s}^{-1}$
Sound pressure amplitude	Δp	10 kPa
Acoustic energy density	$E = \Delta p^2/(2\rho_0 c_f^2)$	22.7 mJ m $^{-3}$
Shear/dynamic viscosity of fluid	ν_s	1.002 mPa s
Bulk/volume viscosity of fluid	ν_b	2.87 mPa s
Inlet-particle or particle-outlet distance	l_1	$\lambda/4$
Inlet length	l_2	200 μm
Mesh-cell size	Δx	15 nm-1 μm
Time-step size	Δt	1-10 ps
Simulation duration	t_{max}	500 τ

TABLE II. Parameters that are relevant for our simulations and their values. The values of the speed of sound c_f , mean mass density ρ_0 , shear viscosity ν_s , and bulk viscosity ν_b are calculated for quiescent water at standard temperature T_0 and standard pressure p_0 , where the value of ν_b is determined by a cubic spline interpolation of the data from Tab. 1 in Ref. [80].

Navier-Stokes equations, and a linear constitutive equation for the fluid's pressure field. These direct fluid dynamics simulations are performed using the finite volume software package OpenFOAM [81].

The simulations first yield the time-dependent force and torque acting on the particle as well as the flow field in the fluid. We calculate this force in the laboratory frame. The force and torque can be calculated from the stress tensor $\Sigma = \Sigma^{(p)} + \Sigma^{(v)}$ of the fluid. This stress tensor consists of a pressure contribution $\Sigma^{(p)}$ and a viscous contribution $\Sigma^{(v)}$ so that the force and torque acting on the particle can be written as sums $\vec{F}^{(p)} + \vec{F}^{(v)}$ and $T^{(p)} + T^{(v)}$, respectively, where $\vec{F}^{(p)}$ and $T^{(p)}$ are the contributions of $\Sigma^{(p)}$ and $\vec{F}^{(v)}$ and $T^{(v)}$ are the contributions of $\Sigma^{(v)}$. The expressions for the contributions to the force and torque are [82]

$$F_i^{(\alpha)} = \sum_{j=1}^2 \int_{\partial\Omega_p} \Sigma_{ij}^{(\alpha)} dA_j, \quad (7)$$

$$T^{(\alpha)} = \sum_{j,k,l=1}^2 \int_{\partial\Omega_p} \epsilon_{ijk} (x_j - x_{p,j}) \Sigma_{kl}^{(\alpha)} dA_l \quad (8)$$

with $\alpha \in \{p, v\}$, the normal and outwards oriented element $d\vec{A}(\vec{x}) = (dA_1(\vec{x}), dA_2(\vec{x}))^T$ of the particle surface $\partial\Omega_p$ at position $\vec{x} \in \partial\Omega_p$, the Levi-Civita symbol ϵ_{ijk} , and the center-of-mass position \vec{x}_p of the particle. Dur-

ing a simulation, the particle is held in its position and orientation. The forces $\vec{F}^{(p)}$ and $\vec{F}^{(v)}$ and torques $T^{(p)}$ and $T^{(v)}$, therefore, correspond to a fixed particle or a particle with infinite mass density, which can be seen as limiting case for a particle with a large mass density.

We average the forces and torques over one period $\tau = 1/f = 1\mu\text{s}$ for large times t and extrapolate $t \rightarrow \infty$ using the extrapolation procedure that is described in Ref. [43] to obtain the forces and torques corresponding to the stationary state. This results in the mean propulsion force $\vec{F} = \vec{F}_p + \vec{F}_v$ with contributions $\vec{F}_p = \langle \vec{F}^{(p)} \rangle$ and $\vec{F}_v = \langle \vec{F}^{(v)} \rangle$ as well as the mean propulsion torque $T = T_p + T_v$ with contributions $T_p = \langle T^{(p)} \rangle$ and $T_v = \langle T^{(v)} \rangle$, where $\langle \cdot \rangle$ denotes the time average. The components F_{\parallel} and F_{\perp} of the propulsion force that are parallel and perpendicular to the particle orientation, respectively, are calculated by the projection

$$F_{\parallel} = \vec{F} \cdot \hat{n}_{\parallel}, \quad (9)$$

$$F_{\perp} = \vec{F} \cdot \hat{n}_{\perp}. \quad (10)$$

We are also interested in the translational velocities v_{\parallel} and v_{\perp} and the angular velocity ω that correspond to F_{\parallel} , F_{\perp} , and T . They can be calculated with the Stokes law [83]

$$\vec{v} = \frac{1}{\nu_s} \mathbf{H}^{-1} \vec{\mathfrak{F}}, \quad (11)$$

where $\vec{v} = (v_{\perp}, v_{\parallel}, 0, 0, 0, \omega)^T$ is a translational-angular velocity vector, $\vec{\mathfrak{F}} = (F_{\perp}, F_{\parallel}, 0, 0, 0, T)^T$ a force-torque vector, ν_s the shear viscosity of the fluid, and

$$\mathbf{H} = \begin{pmatrix} \mathbf{K} & \mathbf{C}_S^T \\ \mathbf{C}_S & \Omega_S \end{pmatrix} \quad (12)$$

the hydrodynamic resistance matrix of the particle for $\theta = \pi/2$. In this matrix, \mathbf{K} , \mathbf{C}_S , and Ω_S are submatrices and the subscript S denotes the reference point for the calculation of \mathbf{H} , which is chosen here as the center of mass. The matrix values are calculated with the software HydResMat [84, 85]. Since the matrix \mathbf{H} corresponds to a three-dimensional particle, but we perform here simulations in two spatial dimensions to keep the computational effort manageable, we assign a thickness of σ of the particle in the third dimension. This leads to the submatrices

$$\mathbf{K} = \begin{pmatrix} 7.74\mu\text{m} & 0 & 0 \\ 0 & 7.48\mu\text{m} & 0 \\ 0 & 0 & 7.16\mu\text{m} \end{pmatrix}, \quad (13)$$

$$\mathbf{C}_S = \begin{pmatrix} 0 & 0 & 0.05\mu\text{m}^2 \\ 0 & 0 & 0 \\ -0.11\mu\text{m}^2 & 0 & 0 \end{pmatrix}, \quad (14)$$

$$\Omega_S = \begin{pmatrix} 1.81\mu\text{m}^3 & 0 & 0 \\ 0 & 1.69\mu\text{m}^3 & 0 \\ 0 & 0 & 1.73\mu\text{m}^3 \end{pmatrix}. \quad (15)$$

From the hydrodynamic resistance matrix \mathbf{H} , we can also calculate the diffusion coefficient $\mathcal{D} = (k_B T_0 / \nu_s) \mathbf{H}^{-1}$ of the particle, where k_B is the Boltzmann constant. The particle's rotational diffusion coefficient, corresponding to rotation in the x_1 - x_2 plane, is then given by $D_R = (\mathcal{D})_{33}$.

To estimate the numerical error that is associated with our results for v_{\parallel} and v_{\perp} , we make use of the fact that the results for the forces \vec{F}_p and \vec{F}_v are, due to the numerical inaccuracies of the calculations, not exactly zero for $\theta = 0$ and $\theta = \pi$, although they should be for reasons of symmetry. We therefore choose the absolute values of \vec{F}_p and \vec{F}_v for $\theta = 0$ and $\theta = \pi$ as estimates for the errors that correspond to \vec{F}_p and \vec{F}_v . Considering the propagation of uncertainty, we then obtain from the estimated errors of \vec{F}_p and \vec{F}_v an estimate for the error of \vec{F} for $\theta = 0$ and $\theta = \pi$ each. Next, we choose the maximum of the estimated errors for both angles as an estimate for the error that corresponds to \vec{F} . Finally, we calculate from this error the error that is associated with v_{\parallel} and v_{\perp} . This error is shown in Fig. 1 as error bars for v_{\parallel} and v_{\perp} .

Nondimensionalization of the equations governing our simulations leads to four dimensionless characteristic numbers: a Reynolds number Re_s corresponding to the shear viscosity ν_s of the fluid

$$\text{Re}_s = \frac{\rho_0 c_f \sigma}{\nu_s} \approx 1045, \quad (16)$$

a Reynolds number Re_b corresponding to the bulk viscosity ν_b of the fluid

$$\text{Re}_b = \frac{\rho_0 c_f \sigma}{\nu_b} \approx 365, \quad (17)$$

the Helmholtz number

$$\text{He} = \frac{2\pi f \sigma}{c_f} \approx 2.99 \cdot 10^{-3}, \quad (18)$$

and the product $\text{Ma}^2 \text{Eu}$ with the Mach number Ma and

Euler number Eu

$$\text{Ma}^2 \text{Eu} = \frac{\Delta p}{\rho_0 c_f^2} \approx 4.55 \cdot 10^{-6}. \quad (19)$$

Note that the largest Reynolds number describing the particle motion through the fluid is close to zero:

$$\text{Re} = \frac{\rho_0 \sigma}{\nu_s} \max_{\theta \in [0, \pi]} \left\{ \sqrt{v_{\parallel}^2(\theta) + v_{\perp}^2(\theta)} \right\} < 10^{-7}. \quad (20)$$

We discretize the fluid domain as a structured mixed rectangle-triangle mesh. It has about 250,000 cells and the typical cell size Δx ranges from 15 nm close to the particle to 1 μm far away from the particle. For the time integration, an adaptive time-step method is used. The maximum time-step size is chosen such that the Courant-Friedrichs-Lewy number

$$C = c_f \frac{\Delta t}{\Delta x} \quad (21)$$

is smaller than one. This leads to a time-step size Δt between 1 ps and 10 ps. For getting close to the stationary state, each simulation runs for $t_{\text{max}} = 500\tau$ or more. Because of the fine discretization in space and time compared to the large temporal and spatial domains of the system, a typical simulation needs about 36,000 CPU core hours.

CONFLICTS OF INTEREST

There are no conflicts of interest to declare.

ACKNOWLEDGMENTS

We thank Patrick Kurzeja for helpful discussions. R.W. is funded by the Deutsche Forschungsgemeinschaft (DFG, German Research Foundation) – WI 4170/3-1. The simulations for this work were performed on the computer cluster PALMA II of the University of Münster.

-
- [1] W. Wang, L. Castro, M. Hoyos, and T. E. Mallouk, “Autonomous motion of metallic microrods propelled by ultrasound,” *ACS Nano* **6**, 6122–6132 (2012).
 - [2] C. Bechinger, R. Di Leonardo, H. Löwen, C. Reichhardt, G. Volpe, and G. Volpe, “Active particles in complex and crowded environments,” *Reviews of Modern Physics* **88**, 045006 (2016).
 - [3] T. Xu, L. Xu, and X. Zhang, “Ultrasound propulsion of micro-/nanomotors,” *Applied Materials Today* **9**, 493–503 (2017).
 - [4] P. Venugopalan, B. Esteban-Fernández de Ávila, M. Pal, A. Ghosh, and J. Wang, “Fantastic voyage of nanomotors into the cell,” *ACS Nano* **14**, 9423–9439 (2020).
 - [5] M. Fernández-Medina, M. A. Ramos-Docampo, O. Hovorka, V. Salgueiriño, and B. Städler, “Recent advances in nano- and micromotors,” *Advanced Functional Materials* **30**, 1908283 (2020).
 - [6] Q. Yang, L. Xu, W. Zhong, Q. Yan, Y. Gao, W. Hong, Y. She, and G. Yang, “Recent advances in motion control of micro/nanomotors,” *Advanced Intelligent Systems* **2**, 2000049 (2020).
 - [7] J. Li, B. Esteban-Fernández de Ávila, W. Gao, L. Zhang, and J. Wang, “Micro/Nanorobots for biomedicine: delivery, surgery, sensing, and detoxification,” *Science Robotics* **2**, eaam6431 (2017).
 - [8] F. Peng, Y. Tu, and D. A. Wilson, “Micro/Nanomotors towards in vivo application: cell, tissue and biofluid,”

- Chemical Society Reviews **46**, 5289–5310 (2017).
- [9] F. Soto and R. Chrostowski, “Frontiers of medical micro/nanorobotics: in vivo applications and commercialization perspectives toward clinical uses,” *Frontiers in Bioengineering and Biotechnology* **6**, 170 (2018).
 - [10] D. Wang, C. Gao, C. Zhou, Z. Lin, and Q. He, “Leukocyte membrane-coated liquid metal nanoswimmers for actively targeted delivery and synergistic chemophotothermal therapy,” *Research* **2020**, 3676954 (2020).
 - [11] W. Wang and C. Zhou, “A journey of nanomotors for targeted cancer therapy: principles, challenges, and a critical review of the state-of-the-art,” *Advanced Healthcare Materials* **10**, 2001236 (2021).
 - [12] M. Luo, Y. Feng, T. Wang, and J. Guan, “Micro-/Nanorobots at work in active drug delivery,” *Advanced Functional Materials* **28**, 1706100 (2018).
 - [13] P. Erkoc, I. C. Yasa, H. Ceylan, O. Yasa, Y. Alapan, and M. Sitti, “Mobile microrobots for active therapeutic delivery,” *Advanced Therapeutics* **2**, 1800064 (2019).
 - [14] Y. Wang, W. Duan, C. Zhou, Q. Liu, J. Gu, H. Ye, M. Li, W. Wang, and X. Ma, “Phoretic liquid metal micro/nanomotors as intelligent filler for targeted microwelding,” *Advanced Materials* **31**, 1905067 (2019).
 - [15] I. Jun and H. Hess, “A biomimetic, self-pumping membrane,” *Advanced Materials* **22**, 4823–4825 (2010).
 - [16] J. McDermott, A. Kar, M. Daher, S. Klara, G. Wang, A. Sen, and D. Velegol, “Self-generated diffusioosmotic flows from calcium carbonate micropumps,” *Langmuir* **28**, 15491–15497 (2012).
 - [17] V. Garcia-Gradilla, J. Orozco, S. Sattayasamitsathit, F. Soto, F. Kuralay, A. Pourazary, A. Katzenberg, W. Gao, Y. Shen, and J. Wang, “Functionalized ultrasound-propelled magnetically guided nanomotors: toward practical biomedical applications,” *ACS Nano* **7**, 9232–9240 (2013).
 - [18] S. Ahmed, W. Wang, L. O. Mair, R. D. Fraleigh, S. Li, L. A. Castro, M. Hoyos, T. J. Huang, and T. E. Mallouk, “Steering acoustically propelled nanowire motors toward cells in a biologically compatible environment using magnetic fields,” *Langmuir* **29**, 16113–16118 (2013).
 - [19] Z. Wu *et al.*, “Turning erythrocytes into functional micromotors,” *ACS Nano* **8**, 12041–12048 (2014).
 - [20] W. Wang, S. Li, L. Mair, S. Ahmed, T. J. Huang, and T. E. Mallouk, “Acoustic propulsion of nanorod motors inside living cells,” *Angewandte Chemie International Edition* **53**, 3201–3204 (2014).
 - [21] V. Garcia-Gradilla, S. Sattayasamitsathit, F. Soto, F. Kuralay, C. Yardımcı, D. Wiitala, M. Galarnyk, and J. Wang, “Ultrasound-propelled nanoporous gold wire for efficient drug loading and release,” *Small* **10**, 4154–4159 (2014).
 - [22] A. L. Balk, L. O. Mair, P. P. Mathai, P. N. Patrone, W. Wang, S. Ahmed, T. E. Mallouk, J. A. Liddle, and S. M. Stavis, “Kilohertz rotation of nanorods propelled by ultrasound, traced by microvortex advection of nanoparticles,” *ACS Nano* **8**, 8300–8309 (2014).
 - [23] S. Ahmed, D. T. Gentekos, C. A. Fink, and T. E. Mallouk, “Self-assembly of nanorod motors into geometrically regular multimers and their propulsion by ultrasound,” *ACS Nano* **8**, 11053–11060 (2014).
 - [24] B. Esteban-Fernández de Ávila, A. Martín, F. Soto, M. A. Lopez-Ramirez, S. Campuzano, G. M. Vázquez-Machado, W. Gao, L. Zhang, and J. Wang, “Single cell real-time miRNAs sensing based on nanomotors,” *ACS Nano* **9**, 6756–6764 (2015).
 - [25] Z. Wu, T. Li, W. Gao, W. Xu, B. Jurado-Sánchez, J. Li, W. Gao, Q. He, L. Zhang, and J. Wang, “Cell-membrane-coated synthetic nanomotors for effective biodegradation,” *Advanced Functional Materials* **25**, 3881–3887 (2015).
 - [26] Z. Wu, B. Esteban-Fernández de Ávila, A. Martín, C. Christianson, W. Gao, S. K. Thamphiwatana, A. Escarpa, Q. He, L. Zhang, and J. Wang, “RBC micromotors carrying multiple cargos towards potential therapeutic applications,” *Nanoscale* **7**, 13680–13686 (2015).
 - [27] K. J. Rao, F. Li, L. Meng, H. Zheng, F. Cai, and W. Wang, “A force to be reckoned with: a review of synthetic microswimmers powered by ultrasound,” *Small* **11**, 2836–2846 (2015).
 - [28] B. Esteban-Fernández de Ávila, C. Angell, F. Soto, M. A. Lopez-Ramirez, D. F. Báez, S. Xie, J. Wang, and Y. Chen, “Acoustically propelled nanomotors for intracellular siRNA delivery,” *ACS Nano* **10**, 4997–5005 (2016).
 - [29] F. Soto, G. L. Wagner, V. Garcia-Gradilla, K. T. Gillespie, D. R. Lakshminpathy, E. Karshalev, C. Angell, Y. Chen, and J. Wang, “Acoustically propelled nanoshells,” *Nanoscale* **8**, 17788–17793 (2016).
 - [30] S. Ahmed, W. Wang, L. Bai, D. T. Gentekos, M. Hoyos, and T. E. Mallouk, “Density and shape effects in the acoustic propulsion of bimetallic nanorod motors,” *ACS Nano* **10**, 4763–4769 (2016).
 - [31] D. Ahmed, T. Baasch, B. Jang, S. Pane, J. Dual, and B. J. Nelson, “Artificial swimmers propelled by acoustically activated flagella,” *Nano Letters* **16**, 4968–4974 (2016).
 - [32] M. Uygun, B. Jurado-Sánchez, D. A. Uygun, V. V. Singh, L. Zhang, and J. Wang, “Ultrasound-propelled nanowire motors enhance asparaginase enzymatic activity against cancer cells,” *Nanoscale* **9**, 18423–18429 (2017).
 - [33] M. Kaynak, A. Ozcelik, A. Nourhani, P. E. Lammert, V. H. Crespi, and T. J. Huang, “Acoustic actuation of bioinspired microswimmers,” *Lab on a Chip* **17**, 395–400 (2017).
 - [34] B. Esteban-Fernández de Ávila, D. E. Ramírez-Herrera, S. Campuzano, P. Angsantikul, L. Zhang, and J. Wang, “Nanomotor-enabled pH-responsive intracellular delivery of caspase-3: toward rapid cell apoptosis,” *ACS Nano* **11**, 5367–5374 (2017).
 - [35] M. Hansen-Bruhn, B. Esteban-Fernández de Ávila, M. Beltrán-Gastélum, J. Zhao, D. E. Ramírez-Herrera, P. Angsantikul, K. Vesterager Gothelf, L. Zhang, and J. Wang, “Active intracellular delivery of a Cas9/sgRNA complex using ultrasound-propelled nanomotors,” *Angewandte Chemie International Edition* **57**, 2657–2661 (2018).
 - [36] S. Sabrina, M. Tasinkevych, S. Ahmed, A. M. Brooks, M. Olvera de la Cruz, T. E. Mallouk, and K. J. M. Bishop, “Shape-directed microspinners powered by ultrasound,” *ACS Nano* **12**, 2939–2947 (2018).
 - [37] D. Wang, C. Gao, W. Wang, M. Sun, B. Guo, H. Xie, and Q. He, “Shape-transformable, fusible rodlike swimming liquid metal nanomachine,” *ACS Nano* **12**, 10212–10220 (2018).
 - [38] B. Esteban-Fernández de Ávila, P. Angsantikul, D. E. Ramírez-Herrera, F. Soto, H. Teymourian, D. Dehaini,

- Y. Chen, L. Zhang, and J. Wang, "Hybrid biomembrane-functionalized nanorobots for concurrent removal of pathogenic bacteria and toxins," *Science Robotics* **3**, eaat0485 (2018).
- [39] X. Lu, H. Shen, Z. Wang, K. Zhao, H. Peng, and W. Liu, "Micro/Nano machines driven by ultrasound power sources," *Chemistry – An Asian Journal* **14**, 2406–2416 (2019).
- [40] J. R. Qualliotine, G. Bolat, M. Beltrán-Gastélum, B. Esteban-Fernández de Ávila, J. Wang, and J. A. Califano, "Acoustic nanomotors for detection of human papillomavirus-associated head and neck cancer," *Otolaryngology–Head and Neck Surgery* **161**, 814–822 (2019).
- [41] C. Gao, Z. Lin, D. Wang, Z. Wu, H. Xie, and Q. He, "Red blood cell-mimicking micromotor for active photodynamic cancer therapy," *ACS Applied Materials & Interfaces* **11**, 23392–23400 (2019).
- [42] L. Ren, N. Nama, J. M. McNeill, F. Soto, Z. Yan, W. Liu, W. Wang, J. Wang, and T. E. Mallouk, "3D steerable, acoustically powered microswimmers for single-particle manipulation," *Science Advances* **5**, eaax3084 (2019).
- [43] J. Voß and R. Wittkowski, "On the shape-dependent propulsion of nano- and microparticles by traveling ultrasound waves," *Nanoscale Advances* **2**, 3890–3899 (2020).
- [44] J. Voß and R. Wittkowski, "Acoustically propelled nano- and microcones: fast forward and backward motion," preprint, arXiv:2102.06438 (2021).
- [45] A. Aghakhani, O. Yasa, P. Wrede, and M. Sitti, "Acoustically powered surface-slipping mobile microrobots," *Proceedings of the National Academy of Sciences U.S.A.* **117**, 3469–3477 (2020).
- [46] J. Liu and H. Ruan, "Modeling of an acoustically actuated artificial micro-swimmer," *Bioinspiration & Biomimetics* **15**, 036002 (2020).
- [47] C. Zhou, J. Yin, C. Wu, L. Du, and Y. Wang, "Efficient target capture and transport by fuel-free micromotors in a multichannel microchip," *Soft Matter* **13**, 8064–8069 (2017).
- [48] C. Zhou, L. Zhao, M. Wei, and W. Wang, "Twists and turns of orbiting and spinning metallic microparticles powered by megahertz ultrasound," *ACS Nano* **11**, 12668–12676 (2017).
- [49] M. Valdez-Garduño, M. Leal-Estrada, E. S. Oliveros-Mata, D. I. Sandoval-Bojorquez, F. Soto, J. Wang, and V. Garcia-Gradilla, "Density asymmetry driven propulsion of ultrasound-powered Janus micromotors," *Advanced Functional Materials* **30**, 2004043 (2020).
- [50] G. Dumy, N. Jeger-Madiot, X. Benoit-Gonin, T. Mallouk, M. Hoyos, and J. Aider, "Acoustic manipulation of dense nanorods in microgravity," *Microgravity Science and Technology* **32**, 1159–1174 (2020).
- [51] B. Esteban-Fernández de Ávila, P. Angsantikul, J. Li, W. Gao, L. Zhang, and J. Wang, "Micromotors go in vivo: from test tubes to live animals," *Advanced Functional Materials* **28**, 1705640 (2018).
- [52] M. Safdar, S. U. Khan, and J. Jänis, "Progress toward catalytic micro- and nanomotors for biomedical and environmental applications," *Advanced Materials* **30**, 1703660 (2018).
- [53] D. Kagan, M. J. Benchimol, J. C. Claussen, E. Chuluun-Erdene, S. Esener, and J. Wang, "Acoustic droplet vaporization and propulsion of perfluorocarbon-loaded microbullets for targeted tissue penetration and deformation," *Angewandte Chemie International Edition* **51**, 7519–7522 (2012).
- [54] M. Xuan, J. Shao, C. Gao, W. Wang, L. Dai, and Q. He, "Self-propelled nanomotors for thermomechanically percolating cell membranes," *Angewandte Chemie International Edition* **57**, 12463–12467 (2018).
- [55] Z. Xu, M. Chen, H. Lee, S.-P. Feng, J. Y. Park, S. Lee, and J. T. Kim, "X-ray-powered micromotors," *ACS Applied Materials & Interfaces* **11**, 15727–15732 (2019).
- [56] F. Nadal and E. Lauga, "Asymmetric steady streaming as a mechanism for acoustic propulsion of rigid bodies," *Physics of Fluids* **26**, 082001 (2014).
- [57] D. Ahmed, M. Lu, A. Nourhani, P. E. Lammert, Z. Stratton, H. S. Muddana, V. H. Crespi, and T. J. Huang, "Selectively manipulable acoustic-powered microswimmers," *Scientific Reports* **5**, 9744 (2015).
- [58] W. Wang, W. Duan, Z. Zhang, M. Sun, A. Sen, and T. E. Mallouk, "A tale of two forces: simultaneous chemical and acoustic propulsion of bimetallic micromotors," *Chemical Communications* **51**, 1020–1023 (2015).
- [59] K. Kim, J. Guo, Z. Liang, F. Zhu, and D. Fan, "Man-made rotary nanomotors: a review of recent developments," *Nanoscale* **8**, 10471–10490 (2016).
- [60] M. Kaynak, A. Ozcelik, N. Nama, A. Nourhani, P. E. Lammert, V. H. Crespi, and T. J. Huang, "Acoustofluidic actuation of in situ fabricated microrotors," *Lab on a Chip* **16**, 3532–3537 (2016).
- [61] L. Ren, D. Zhou, Z. Mao, P. Xu, T. J. Huang, and T. E. Mallouk, "Rheotaxis of bimetallic micromotors driven by chemical-acoustic hybrid power," *ACS Nano* **11**, 10591–10598 (2017).
- [62] J. F. Collis, D. Chakraborty, and J. E. Sader, "Autonomous propulsion of nanorods trapped in an acoustic field," *Journal of Fluid Mechanics* **825**, 29–48 (2017).
- [63] X.-Z. Chen, B. Jang, D. Ahmed, C. Hu, C. De Marco, M. Hoop, F. Mushtaq, B. J. Nelson, and S. Pané, "Small-scale machines driven by external power sources," *Advanced Materials* **30**, 1705061 (2018).
- [64] L. Ren, W. Wang, and T. E. Mallouk, "Two forces are better than one: combining chemical and acoustic propulsion for enhanced micromotor functionality," *Accounts of Chemical Research* **51**, 1948–1956 (2018).
- [65] D. Zhou, Y. Gao, J. Yang, Y. C. Li, G. Shao, G. Zhang, T. Li, and L. Li, "Light-ultrasound driven collective "firework" behavior of nanomotors," *Advanced Science* **5**, 1800122 (2018).
- [66] S. Tang *et al.*, "Structure-dependent optical modulation of propulsion and collective behavior of acoustic/light-driven hybrid microbowls," *Advanced Functional Materials* **29**, 1809003 (2019).
- [67] J. Li, T. Li, T. Xu, M. Kiristi, W. Liu, Z. Wu, and J. Wang, "Magneto-acoustic hybrid nanomotor," *Nano Letters* **15**, 4814–4821 (2015).
- [68] J. Voß and R. Wittkowski, Supplementary Data, Zenodo, DOI: 10.5281/zenodo.4604562 (2021).
- [69] H. Bruus, "Acoustofluidics 7: The acoustic radiation force on small particles," *Lab on a Chip* **12**, 1014–1021 (2012).
- [70] S. B. Barnett, G. R. Ter Haar, M. C. Ziskin, H. D. Rott, F. A. Duck, and K. Maeda, "International recommendations and guidelines for the safe use of diagnostic ultrasound in medicine," *Ultrasound in Medicine & Biology* **26**, 355–366 (2000).

- [71] A. Sprenger, M. Fernandez-Rodriguez, L. Alvarez, L. Isa, R. Wittkowski, and H. Löwen, “Active Brownian motion with orientation-dependent motility: theory and experiments,” *Langmuir* **36**, 7066–7073 (2020).
- [72] R. Wittkowski and H. Löwen, “Self-propelled Brownian spinning top: dynamics of a biaxial swimmer at low Reynolds numbers,” *Physical Review E* **85**, 021406 (2012).
- [73] B. ten Hagen, R. Wittkowski, D. Takagi, F. Kümmel, C. Bechinger, and H. Löwen, “Can the self-propulsion of anisotropic microswimmers be described by using forces and torques?” *Journal of Physics: Condensed Matter* **27**, 194110 (2015).
- [74] J. Bickmann and R. Wittkowski, “Predictive local field theory for interacting active Brownian spheres in two spatial dimensions,” *Journal of Physics: Condensed Matter* **32**, 214001 (2020).
- [75] J. Bickmann and R. Wittkowski, “Collective dynamics of active Brownian particles in three spatial dimensions: a predictive field theory,” *Physical Review Research* **2**, 033241 (2020).
- [76] M. te Vrugt, H. Löwen, and R. Wittkowski, “Classical dynamical density functional theory: from fundamentals to applications,” *Advances in Physics* **69**, 121–247 (2020).
- [77] R. Wittkowski, J. Stenhammar, and M. E. Cates, “Nonequilibrium dynamics of mixtures of active and passive colloidal particles,” *New Journal of Physics* **19**, 105003 (2017).
- [78] J. Jeggle, J. Stenhammar, and R. Wittkowski, “Pair-distribution function of active Brownian spheres in two spatial dimensions: simulation results and analytic representation,” *Journal of Chemical Physics* **152**, 194903 (2020).
- [79] S. Bröker, J. Stenhammar, and R. Wittkowski, “Pair-distribution function of active Brownian particles in three spatial dimensions,” in preparation (2021).
- [80] M. J. Holmes, N. G. Parker, and M. J. W. Povey, “Temperature dependence of bulk viscosity in water using acoustic spectroscopy,” *Journal of Physics: Conference Series* **269**, 012011 (2011).
- [81] H. G. Weller, G. Tabor, H. Jasak, and C. Fureby, “A tensorial approach to computational continuum mechanics using object-oriented techniques,” *Computers in Physics* **12**, 620–631 (1998).
- [82] L. D. Landau and E. M. Lifshitz, *Fluid Mechanics*, 2nd ed., Landau and Lifshitz: Course of Theoretical Physics, Vol. 6 (Butterworth-Heinemann, Oxford, 1987).
- [83] J. Happel and H. Brenner, *Low Reynolds Number Hydrodynamics: With Special Applications to Particulate Media*, 2nd ed., Mechanics of Fluids and Transport Processes, Vol. 1 (Kluwer Academic Publishers, Dordrecht, 1991).
- [84] J. Voß and R. Wittkowski, “Hydrodynamic resistance matrices of colloidal particles with various shapes,” preprint, arXiv:1811.01269 (2018).
- [85] J. Voß, J. Jeggle, and R. Wittkowski, “HydResMat – FEM-based code for calculating the hydrodynamic resistance matrix of an arbitrarily-shaped colloidal particle,” Zenodo (2019), DOI: 10.5281/zenodo.3541588.